Robust and Gain-Scheduled Flight Control of Fixed-Wing UAVs in Wind and Icing Conditions

Ruben Kleiven Kristoffer Gryte Tor Arne Johansen
Norwegian University of Science and Technology
Trondheim, Norway

***Abstract*—Simulations of a fixed-wing unmanned aerial vehicle with varying degrees of icing, both symmetric and asymmetric, and both ice accretion and ice shedding, show the applicability of robust H_∞ inner-loop control for both the lateral and the longitudinal axes to extend the flight envelope. A gain-scheduled extension of the controller compares favourably in performance, at the cost of complexity and needing to know current the icing level. The results also show that higher airspeeds reduces the disturbance related to instantaneous removal of ice. A simple analysis of the open-loop dynamics of the aerodynamic model show that only the spiral-mode eigenvalue moves into the right hand plane with increased icing levels.**

TABLE OF CONTENTS

1. INTRODUCTION

The application areas for fixed-wing unmanned aerial vehicles (UAVs) have increased extensively throughout the past decades, and they have already proven useful in military, scientific and civil applications. With the increased use comes increased requirements, such as all-weather capabilities. This includes environmental conditions such as strong wind and atmospheric icing. Atmospheric icing occurs when supercooled water droplets in clouds freeze on impact with the aircraft surface, and is a topic of that still sees a lot of research since it severely reduce the performance of the UAVs, thus limiting operations, and since it leads to loss of UAVs each year, [1]. Small UAVs are not only more exposed to icing than larger aircraft, as they more often operate in regions with icing conditions, but their limited size and limited resources availability makes some de-icing and anti-icing techniques less convenient.

Both the build-up of ice and the shedding induced by the de-icing system change the UAV dynamics substantially. With more ice build-up the drag is increased while thrust is reduced, and lift is decreased while the weight increases [2]. This reduces the flight envelope, and lowers stability margins. With the shedding of ice, the effects are reversed, but the change in dynamics is both more abrupt and may temporarily lead to a UAV with severe lateral asymmetry, which can be challenging to the controller. As using anti-icing and de-icing systems are potentially resource-demanding (e.g. electric power consumption using electro-thermal icing protection, [3]), it is also interesting to increase the UAVs tolerance to ice build-up, by introducing a more robust controller, such that the use of the ice protection system can be reduced.

While most previous research results within UAV icing has focused on mitigation and detection, this work assumes that the icing level is given, and instead focus on the control problem and the UAV dynamics in icing by investigating if the use of robust and gain-scheduled low-level controllers can stabilize the UAV airframe, despite being subject to both symmetric and asymmetric build-up and shedding of ice. Both the robust controller and the gain-scheduled controller are based on $\mathcal{H}_\infty$ control approach, rely on a systematic loop-shaping design procedure for tuning, and are tested through numerical simulations in different wind, airspeed and icing conditions. To investigate the robustness against the possible asymmetries that could be introduced by the de-icing system, a simple asymmetric adaptation of the model from [4] is made. We note that the effects of icing on control surfaces and propeller are not considered in this study.

Organization— This paper starts by presenting modelling of UAVs in icing, and an eigenvalue anaysis of the presented model, in section 2. The main contribution comes in section 3, where the single- and the gain-scheduled H_∞ controllers are presented and adapted to the UAV icing problem. Section 4 presents the simulation results, where the controllers are compared to each other and tested in various icing conditions, before conclusions are drawn in section 5.

2. MODELLING OF UAV IN ICE

This work models UAVs similarly to what is found in the litterature [5], [6], with the addition of icing effects as introduced in [4]. By denoting the icing level variable as $\zeta \in [0, 1]$, describing the level of icing, where $\zeta = 0$ indicates no ice (referred to as clean) and $\zeta = 1$ indicates the worst-case level of ice (referred to as iced). The model is extended to include icing effects by using linear interpolation between the clean and iced case for the aerodynamic coefficients. This includes all the partial derivatives and the non-linear coefficients depending on the angle of sideslip or angle of attack. The general coefficient C_k given as a function of the icing level ζ:

$$C_k(\zeta) = C_{k,0} + \zeta(C_{k,1} - C_{k,0}) \tag{1}$$

Here, $C_{k,0}$ is the coefficient value for the clean case and $C_{k,1}$ is the value for the fully iced case. Since the ice aggregation largely occurs on the leading edge of the wings, the control effectiveness coefficients, $C_{k_{\delta_*}}$ corresponding to trailing edge deflections, are assumed unaffected by the icing.

Corresponding author K. Gryte kristoffer.gryte@ntnu.no
978-1-6654-3760-8/22/$31.00

Asymmetric icing model

To investigate effects of asymmetric ice aggregation and shedding, these effects must be incorporated in the simulation model. The need for extensive CFD analysis in creating such an extension is mitigated by combining the existing, symmetric data from [4] with first-principle assumptions to arrive at an asymmetric model that considers the aerodynamic forces and moments on each wing. While this approach is not expected to be perfect, it will incorporate the asymmetry and highlight some challenges associated with it. The asymmetric aircraft model is obtained by dividing the aerodynamic forces acting on the aircraft into two parts, a left side and a right side. Figure 1 illustrates this division and shows the resulting aerodynamic forces. The forces acting on the right-wing are denoted $\boldsymbol{F}_{k,r}$, where k can be D, S or L for drag-, side- and lift force, respectively. Similarly, $\boldsymbol{F}_{k,l}$ corresponds to left wing forces. The distance vector from the centre of mass to the point of attack on the right-wing is denoted $\boldsymbol{r}_k$. By using the right-wing drag force, $\boldsymbol{F}_{D,r}$ as an example, the distance vector from the centre of mass to the point of attack is denoted $\boldsymbol{r}_D$. Similarly, the distance vector from the centre of mass to a force acting on the left wing is denoted $\boldsymbol{l}_k$. The aerodynamic forces acting through the aircraft centre of mass is found by summarizing over the left and right wing:

$$\boldsymbol{F}_k = \boldsymbol{F}_{k,r} + \boldsymbol{F}_{k,l} \tag{2}$$

The aerodynamic moment is now given by

$$\boldsymbol{M}_{a,\text{asym}} = \boldsymbol{M}_{a,0} \tag{3}$$

$$+ \sum_k (\boldsymbol{r}_k \times \boldsymbol{F}_{k,r} + \boldsymbol{l}_k \times \boldsymbol{F}_{k,l}) \forall \boldsymbol{F}_{k,r}, \boldsymbol{F}_{k,l} \notin \boldsymbol{M}_{a,0}, \tag{4}$$

where $\boldsymbol{M}_{a,0}$ is the nominal moment vector from the symmetric icing model[4]. The second term is caused by asymmetry in corresponding aerodynamic forces on the left and right wing. Note that in order to avoid counting the force contribution twice, the last term is only added if they are not already taken into account as a part of the symmetric case.

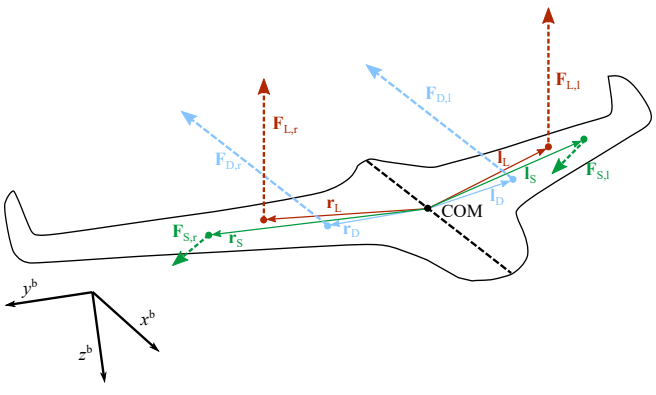

Figure 1. Asymmetric forces aircraft model

The point of attack for the aerodynamic forces acting on the aircraft were not possible to specify based on the symmetric data available. Hence, the points used in later simulations are based on qualified guessing. For simplicity, all points of attacks are assumed to lie on the $\pm$y - axis. This assumption is reasonable, because the largest asymmetric moment contributions, which is from drag force to yaw moment and from lift force to roll moment, are retained. Another assumption made is that icing level does not effect the points of attacks y-coordinate. By combining these assumptions, the relation between distance vector from the centre of mass to the left wing center of pressure, $\mathbf{l_i}$, and right-wing center of pressure, $\mathbf{r_i}$, for $i \in \{D, S, L\}$ is given as

$$\mathbf{l_i} = -\mathbf{r_i} \implies \begin{bmatrix} 0 \\ y_{i,l} \\ 0 \end{bmatrix} = - \begin{bmatrix} 0 \\ y_{i,r} \\ 0 \end{bmatrix} \tag{5}$$

where $y_{i,l}$ and $y_{i,r}$ is the y coordinate of the centre of pressure for left -and right-wing in body frame.

For many UAVs, the fuselage will give a larger contribution to the drag force than the wings. Hence the point of attack for the aircraft drag force will have to lie somewhere between the centre of mass and the middle of the wing. The lift force may be largest at the part of the wing closest to the fuselage and decreases along the wing when the cord length decreases. For the side force, the main contributions are from the fuselage, tail and the winglets. The side force is typically smaller in magnitude than the lift and drag forces. In addition, having the point of attack on the $\pm$y - axis will make the asymmetric moment contribution from the side force small.

Dynamic modes analysis

Figure 2 shows the various aerodynamic coefficients dependencies on angle of attack (AOA) and angle of sideslip (AOS) for the UAV considered in the following, the Skywalker X8 flying wing. The green curves are showing icing level $\zeta = 1$, the blue curves are showing icing level $\zeta = 0$ and the red curves are showing the asymmetric case with icing levels $\zeta = 0$ and $\zeta = 1$ on the left- and right-wing respectively.

Figure 2 also illustrates the general effects of icing. It is clear that the drag force is increased, and the lift force is decreased with icing. These effects increase with the angle of attack. It is also worth noticing that the roll-off in the lift coefficient starts at a lower angle of attack when ice is present. As a consequence, the angle where the lift coefficient exceeds the value which creates maximum lift, also known as stall angle, is lower for the iced case. Figure 2 illustrates that the effect of icing on the lift coefficient at low angles of attack is small. Since the largest effects of icing conditions are on the drag and lift force in the symmetric case, it is clear that the effects of symmetric icing are primarily in the longitudinal direction. The asymmetric effects for the lateral aerodynamic functions are more significant. As illustrated in fig. 2a, these functions are very dependant on the drag and lift forces. This lead to increased cross-coupling between the lateral and longitudinal dynamics.

When comparing icing-induced changes of the dynamic system to the basic clean case uav, it is suitable to analyze the characteristics of the dynamic modes. By linearizing the non-linear aircraft dynamics at a given operating point, the eigenvalues can be found and used to determine the aircraft stability properties at this operating condition. This analysis is performed at trim points for low ($\alpha \approx 2.14\,\text{deg}$) and high ($\alpha \approx 7.5\,\text{deg}$) angles of attack. The airspeed is approximately 21 m/s for the low angle of attack and 13 m/s for the high angle of attack. Figure 3a and fig. 3b shows how the lateral and longitudinal eigenvalues are affected at the trim point for a low angle of attack. Here, the filled circle denotes the eigenvalue in the clean case, and the cross

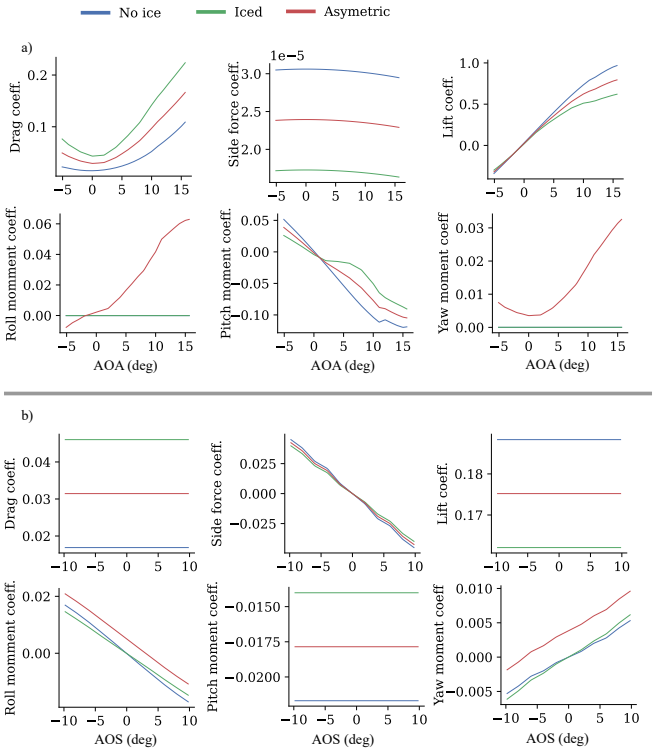

Figure 2. aerodynamic functions

denotes the eigenvalue in the fully iced case. The line shows the intermediate eigenvalues.

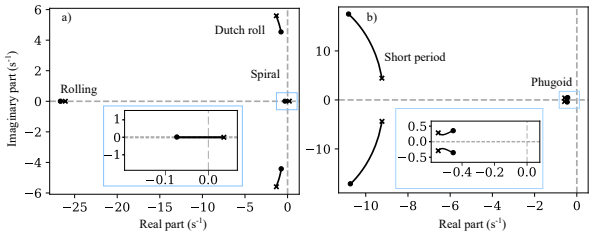

Figure 3. Dynamic modes in icing conditions at $\alpha \approx 2.14°$ for *a)*: lateral and *b)*: longitudinal. The circle denotes the eigenvalue in the clean case, and the cross denotes the eigenvalue in the iced case.

The qualitative development of the eigenvalues as a function of the icing level is similar in the case of high and low angles of attacks. That is, the spiral mode moves from the left half-plane to the right half-plane, the other negative non-complex eigenvalues stays negative non-complex, and the negative complex-eigenvalues stays negative complex for all levels of ice at both low and high angles of attack. The longitudinal eigenvalues for the clean and fully iced case at high and low angles of attack are given by

$$\begin{aligned} \text{ev}_{\text{lon}}(\alpha \approx 7.52°, \text{iced}) &= \begin{cases} -5.482 \pm 8.043i \\ -0.364 \pm 0.672i \end{cases} \\ \text{ev}_{\text{lon}}(\alpha \approx 7.45°, \text{clean}) &= \begin{cases} -5.892 \pm 9.645i \\ -0.255 \pm 0.483i \end{cases} \end{aligned} \tag{6a}$$

$$\begin{aligned} \text{ev}_{\text{lon}}(\alpha \approx 2.14°, \text{iced}) &= \begin{cases} -9.235 \pm 4.565i \\ -0.544 \pm 0.277i \end{cases} \\ \text{ev}_{\text{lon}}(\alpha \approx 2.14°, \text{clean}) &= \begin{cases} -10.745 \pm 17.245i \\ -0.459 \pm 0.345i \end{cases} \end{aligned} \tag{6b}$$

The largest change here is that for the low angle of attacks, the short period mode is considerably less damped in the clean case than in the iced case. The same effect on a much lower scale can be seen for high angles of attack. The phugoid mode in the iced case moves away further into the left half-plane from the clean case for both high and low angle of attacks. The phugoid damping ratio is increased with both an increase in angle of attack and ice. This may be explained by fact that the phugoid mode is dependant on the drag-to-lift ratio [7]. This ratio is generally changed in icing conditions, primarily due to the significant drag increase. Due to different arispeeds, it is also changed for trim conditions at different angles of attack.

The lateral eigenvalues for the clean and fully iced case at high and low angles of attack are given by

$$\begin{aligned} \text{ev}_{\text{lat}}(\alpha \approx 7.52°, \text{iced}) &= \begin{cases} -15.959 + 0.000i \\ -0.890 \pm 3.562i \\ 0.109 + 0.000i \end{cases} \\ \text{ev}_{\text{lat}}(\alpha \approx 7.45°, \text{clean}) &= \begin{cases} -15.090 + 0.000i \\ -0.518 \pm 2.908i \\ -0.045 + 0.000i \end{cases} \end{aligned} \tag{7a}$$

$$\begin{aligned} \text{ev}_{\text{lat}}(\alpha \approx 2.14°, \text{iced}) &= \begin{cases} -26.231 + 0.000i \\ -1.305 \pm 5.530i \\ 0.034 + 0.000i \end{cases} \\ \text{ev}_{\text{lat}}(\alpha \approx 2.14°, \text{clean}) &= \begin{cases} -26.562 + 0.000i \\ -0.791 \pm 4.552i \\ -0.067 + 0.000i \end{cases} \end{aligned} \tag{7b}$$

In the iced case, the spiral mode moves from the left to the right half-plane. In other words, icing destabilizes the spiral mode. Due to the spiral mode giving rise to very slow dynamic behaviour, it is not too critical to handling. Other than this, the effects of icing are quite small for the lateral dynamics. The dutch roll mode becomes more damped. This can be attributed to the increased drag during icing conditions, which in turn leads to increased local drag differences on the wings during a yawing motion. Consequently, the yawing damping is increased. The rolling mode gets slightly slower in icing condition and moves towards the origin, which indicates higher aerodynamic damping of the rolling motion.

Actuator model

To ensure realistic control, the simulation model also includes actuators, with both static and dynamic limitations. While the static constraints are simple saturations, the dynamic limitations are implemented using a simple first order model

$$\frac{u_a}{u_c} = \frac{\frac{1}{\tau}}{1 + \frac{1}{\tau}s} \tag{8}$$

where τ is the actuator time constant, given by the inverse of the rate limit. The static constraints are handled saturation on the control signals.

3. CONTROLLER DESIGN

$\mathcal{H}_\infty$ Optimal Control

The $\mathcal{H}_\infty$ optimal controller [8]–[10] can be found by formulating the control problem as a mathematical optimization problem, and is typically formulated as in fig. 4 [10], mathematically expressed as

$$\begin{aligned}\dot{\mathbf{x}} &= \mathbf{A}\mathbf{x} + \mathbf{B}\mathbf{u} + \mathbf{E}\mathbf{w} \\ \mathbf{z} &= \mathbf{C_1}\mathbf{x} + \mathbf{D_2}\mathbf{u} + \mathbf{D_1}\mathbf{w} \\ \mathbf{y} &= \mathbf{C_2}\mathbf{x} + \mathbf{D_4}\mathbf{u} + \mathbf{D_3}\mathbf{w},\end{aligned} \tag{9}$$

where $\boldsymbol{x}$ is the state vector, $\boldsymbol{u}$ is the control variables, $\boldsymbol{y}$ is the measured variables, $\boldsymbol{z}$ is the weighted error signals which are to be minimized, and $\boldsymbol{w}$ is the exogenous inputs, including disturbances, sensor noise and reference signals. $\boldsymbol{P}$ is the general plant, whose transfer function is given by

$$\begin{aligned}\mathbf{P}(\mathbf{s}) &= \begin{bmatrix} \mathbf{D_1} & \mathbf{D_2} \\ \mathbf{D_3} & \mathbf{D_4} \end{bmatrix} + \begin{bmatrix} \mathbf{C_1} \\ \mathbf{C_2} \end{bmatrix} (s\boldsymbol{I} - \boldsymbol{A})^{-1} \begin{bmatrix} \mathbf{E} & \mathbf{B} \end{bmatrix} \\ &= \left[\begin{array}{c|c} \mathbf{P_{11}} & \mathbf{P_{12}} \\ \hline \mathbf{P_{21}} & \mathbf{P_{22}} \end{array}\right],\end{aligned} \tag{10}$$

while $\boldsymbol{C}$ is the feedback controller. For a linear controller, $\mathbf{C}(\mathbf{s})$, connected from $\boldsymbol{y}$ to $\boldsymbol{u}$, as shown in fig. 4, the closed loop transfer function from exogenous inputs to the weighted error signal is given by [11]

$$\frac{\mathbf{z}}{\mathbf{w}}(s) = \mathcal{F}(\mathbf{P}, \mathbf{C})(\mathbf{s}) = \mathbf{P_{11}} + \mathbf{P_{12}}\mathbf{C}(\mathbf{I} - \mathbf{P_{22}}\mathbf{C})^{-1}\mathbf{P_{21}} \tag{11}$$

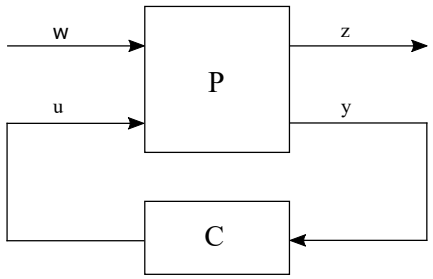

Figure 4. General Control Configuration

The $\mathcal{H}_\infty$ optimized controller seeks to minimize the worst case effects of the exogenous inputs $\mathbf{w}$ on the weighted error signal $\mathbf{z}$, by minimizing $||\mathcal{F}(\mathbf{P}, \mathbf{C})(\mathbf{s})||_\infty = \sup_\omega \bar{\sigma}(\mathcal{F}(\mathbf{P}, \mathbf{C})(\mathbf{j}\omega))$, where $\bar{\sigma}(\cdot)$ denotes the maximum singular value.

Controller Tuning—The tuning parameters of the $\mathcal{H}_\infty$ controller are the weighting filters used on the error signals $\boldsymbol{z}$. By denoting the model plant as $\boldsymbol{G}(s)$, the sensitivity function $\boldsymbol{S}(s)$ and complementary sensitivity function $\boldsymbol{T}(s)$ are defined as;

$$\begin{aligned}\boldsymbol{S}(s) &= (\boldsymbol{I} + \boldsymbol{L}(s))^{-1} \\ \boldsymbol{T}(s) &= \boldsymbol{L}(\boldsymbol{I} + \boldsymbol{L}(s))^{-1},\end{aligned} \tag{12}$$

where $\boldsymbol{L}(s) = \boldsymbol{G}(s)\boldsymbol{C}(s)$ is the open loop transfer function, and $\boldsymbol{I}$ is the identity matrix of the same order as $\boldsymbol{L}(s)$. The error $\boldsymbol{e}(s)$ and measured output $\boldsymbol{y}(s)$ can then be expressed as

$$\begin{aligned}\boldsymbol{e}(s) &= \boldsymbol{S}(s)\boldsymbol{r}(s) \\ \boldsymbol{y}(s) &= \boldsymbol{T}(s)\boldsymbol{r}(s)\end{aligned} \tag{13}$$

Figure 5 shows a block diagram of the system with weighting filters W_S, W_C and W_T, and the weighted sensitivity, control activity and complementary sensitivity z_1, z_2 and z_3. To ensure good reference tracking, it is desirable to have a high complementary sensitivity gain and low sensitivity gain at low frequencies. At high frequencies, it is desirable to have a low complementary sensitivity gain to ensure good noise attenuation and robustness.

There are multiple methods to design weighting filters. Using loop-shaping[8], the weighting filters are used to shape the desired sensitivity and complementary sensitivity frequency responses. In order to avoid unnecessary complex controllers, the weighting filters should be chosen of the lowest order that meets the desired requirements [8]. The transfer functions are limited by the inverse of its corresponding filter, so e.g. $W_s(s)$ should be the inverse of the desired shape of $\boldsymbol{S}(s)$, such that when the $||W_S(s)\boldsymbol{S}(s)||_\infty$, is minimized, it will shape the desired $\boldsymbol{S}(s)$.

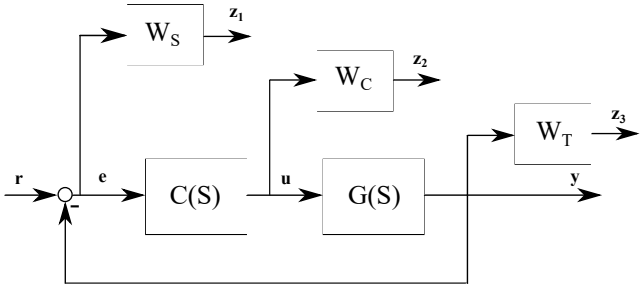

Figure 5. Closed-loop block diagram with weighted error signals.

The general loop-shaping principles on the desired shapes of complementary sensitivity- and sensitivity functions is the foundation of the tuning process. These principles set the general shapes of the filters

$$W_S(s) = \frac{s/M + 1}{s + \omega_0 A} \tag{14a}$$

$$W_C(s) = \text{Constant} \tag{14b}$$

$$W_T(s) = \frac{s + \omega_0/M}{As + \omega_0} \tag{14c}$$

were ω_0 is the desired controller bandwidth, M is limiting the maximum sensitivity peak and A limits the low-frequency gains. Control activity is limited by the $W_C^{-1}(s)$. By choosing W_C as a constant, all control activity is penalized equally at all frequencies. Too low penalty on the control signal may lead to oscillatory responses. Too high penalty on the control signal may limit the closed-loop bandwidth, which in turn gives worse reference tracking.

W_T is usually formed to get sufficient noise attenuation and robustness to uncertain high-frequency dynamics. High-frequency noise is not considered here, so W_T is chosen as a first-order high pass filter with the same crossover frequency as W_S.

There are cases where it is necessary to use higher-order filters, although they results in higher-order controllers. For instance, one can increase the controller integral action by increasing the order of the tuning filters. The general equation for a second-order sensitivity filter is given by

$$W_S = \frac{(s/M^{\frac{1}{2}} + \omega_0)^2}{(s + \omega_0 A^{\frac{1}{2}})^2} \tag{15}$$

Higher-order filters will generally give better disturbance rejection, at the cost of degraded performance in the form of increasing the step-overshoot.

γ-iteration—γ-iteration is a bisection algorithm used to find $\mathcal{H}_\infty$ optimized controller. The γ-iteration method starts with high, γ_{max}, and low, γ_{min}, estimates of γ and iterates on γ-values to find the $\mathcal{H}_\infty$ optimal controller. There are numerical methods used for solving the $\mathcal{H}_\infty$-problem. For the Riccati-based method used in Lavertsky *et al.* [8], this algorithm computes the smallest γ-value, γ_{opt}, within the γ-range for which the stabilizing non-negative definite Riccati-solutions exists. Now, γ_{opt} is the controller performance level, and the following relation is met;

$$||\mathcal{F}(\mathbf{P}, \mathbf{C})(\mathbf{s})||_\infty < \gamma_{\text{opt}} \tag{16}$$

Robust Stability

The Vinnicombe, ν-gap, metric, is a distance measure between two linear time-invariant (LTI) systems[9], [12], [13]. Aircraft in icing condition can be handled as a nominal plant with plant uncertainty. Hence the ν-gap metric can be used as an uncertainty measure between the nominal plant and the plant at a given icing level.

The Vinnicombe distance is defined by

$$\delta_v(P_1, P_2) = \begin{cases} \sup_\omega \frac{|P_1 - P_2|}{\sqrt{(1+P_1P_1^*)(1+P_2P_2^*)}}, \text{if}(P_1, P_2) \in \mathcal{S} \\ 1, \text{otherwise} \end{cases} \tag{17}$$

where $\mathcal{S}$ is the set of all LTI system pairs, (P_1, P_2), that fullfills the winding number condition

$$(1 + P_2^* P_1) \neq 0 \forall \omega \tag{18a}$$

$$\text{wno}(1 + P_2^* P_1) + \eta(P_1) - \eta(P_2) - \eta_0(P_2) = 0 \tag{18b}$$

Here, the winding number, wno, is evaluated along the standard Nyquist contour, $\eta(\cdot)$ denotes the number of unstable poles, $\eta_0(\cdot)$ is the number of poles on the imaginary axis and P_i^* is the conjugated plant P_i.

The robustness of a controller to plant uncertainty can be described by the gap metric stability margin[2]

$$b_{P,C} = \left|\left| \begin{bmatrix} P \\ I \end{bmatrix} (1 - CP)^{-1} \begin{bmatrix} -C & I \end{bmatrix} \right|\right|_\infty^{-1}, \tag{19}$$

[2]Also known as normalized coprime stability margin

Here, $b_{P,C} \in [0, 1]$, where higher stability margin indicates increased robustness to plant perturbations.

Then, given a nominal plant, P, the controller C stabilizes all plants, $P^* \in \mathcal{B}$ on different icing levels, where

$$\mathcal{B} = \{ P^* \mid b_{P,C} > \delta_\nu(P, P^*) \} \tag{20}$$

By having a nominal plant P_0 at a icing level $\zeta \in [0, 1]$, worst-case iced plant P_{ice} at icing level $\zeta = 1$ and plant with no ice P_{clean}, the stability requirement can be stated as

$$b_{P_0,C} > \max(\delta_\nu(P_0, P_{\text{ice}}), \delta_\nu(P_0, P_{\text{clean}})), \tag{21}$$

where $b_{P_0,C}$ is the gap metric stability margin. Assuming that the ν-gap distance between two plants is increasing when the difference in icing level is increasing, the stability criterion implies that the controller stabilizes plants for all icing levels. This assumption is reasonable since the icing model is found by linear interpolation between the iced and clean case.

The lower threshold robustness requirements used in this work are [14]

- Minimum phase margin $\phi_m = 30°$
- Minimum gain margin $g_m = 2$
- Minimum stability margin s_m between $0.5 - 0.8$

Controller Tuning Process

The loop-shaping tuning process can be summarized in the following steps.

- Finding the icing level for the nominal plant that minimizes the maximum ν-gap distance to the extreme cases. The plant at this icing level is used for the controller synthesis. In other words, the nominal plant is chosen to be at the midpoint of the worst-case plants. This choice will give the most relaxed stability requirement, as the right term in eq. (21) will be minimized. This choice is also performance-related. Typically, increasing and decreasing the icing level will give opposite closed-loop performance effects. Either give a more rapid response with a higher overshoot, or a slower response and a lower overshoot. Hence, choosing a midpoint nominal plant will minimize the qualitative differences in closed-loop responses from nominal to worst-case plants.
- Select the desired range of sufficient bandwidth frequencies. Here, the elements of noise attenuation and fundamental limitations like right half plane zeros and time delays should be taken into account when choosing the upper threshold. The lower threshold should be chosen based on minimum performance requirements related to reference tracking.
- Finding filter parameter values in eq. (14) based on an iterative process. A is chosen such that the low-frequency disturbance rejection is sufficient. For SISO systems, the stability margin is given by the maximum peak of the sensitivity transfer function. Hence M is chosen based on the stability margin requirement. ω_0 is chosen to be the minimum frequency in the frequency range chosen in step 2. Then W_C is adjusted such that the system response is non-oscillatory. The robustness-, stability- and performance requirements are then checked for both the worst-case and nominal plants. As long as all the requirements are met, ω_0 is increased, and this step is repeated. The idea is to get as high as possible bandwidth within the target frequency range to achieve good performance while robustness and stability requirements are met.
- If the final controller does not have sufficient disturbance rejection, increase the filter order on the sensitivity function as shown in eq. (15), and repeat the last step.

Note that only plants with symmetric icing are considered in the tuning process, for simplicity. However, the results in section 4 also considers asymmetric icing scenarios.

Gain-Scheduled Control

By switching between several controllers, each designed for different operating points in the operational area, gain-scheduling allows the use of simple linear control methods to control non-linear systems where the dynamics is changing considerably at different operating points [14]. In other words, this approach can be used when a single linear controller does not provide the desired performance and stability for all operating points. For this method to be feasible, the states/variables that change the operating point needs to be measurable, as it is used to select the appropriate controller given the system state. Here, it is vital that the operating point changes slowly and does not introduce undesirable transients or even instability.

Longitudinal control

The inner-loop longitudinal controller sets the desired elevator deflection based on the commanded pitch angle and desired throttle based on commanded airspeed. The longitudinal state space model has state vector and inputs

$$\mathbf{x}_{\text{lon}} = \begin{bmatrix} u \\ w \\ q \\ \theta \end{bmatrix} \quad \mathbf{u}_{\text{lon}} = \begin{bmatrix} \delta_e \\ \delta_t \end{bmatrix}, \tag{22}$$

where u and w are body-frame x- and z-axis velocities, q is pitch rate, θ is pitch angle, δ_e is the elevator deflection and δ_t is the throttle. It can be written as

$$\Delta\dot{\mathbf{x}}_{\text{lon}} = \frac{df_{\text{lon}}}{d\mathbf{x}_{\text{lon}}}\Delta\mathbf{x}_{\text{lon}} + \frac{\mathbf{df}_{\text{lon}}}{\mathbf{du}_{\text{lon}}}\mathbf{\Delta u}_{\text{lon}} \tag{23}$$

The longitudinal open-loop dynamics includes the short period modes and the phugoid modes. The airspeed and pitch angle are two coupled states that are controlled by two control variables. Thrust, δ_t, is the primary airspeed control variable and elevator deflection, δ_e, is the primary pitch control variable. This control problem is approached by having two SISO controllers. As the focus here is on inner-loop control, how the desired pitch angle and airspeed are calculated is considered out of scope.

One of the main effects of icing is increased drag, so the throttle needed to maintain the airspeed is increased, while the maximum obtainable airspeed is lowered. The airspeed controller is implemented as a simple PI controller with anti-windup;

$$\delta_t = \tilde{\delta}_t + (K_p + \frac{K_i}{s})(V_a^c - V_a) \tag{24}$$

where $\tilde{\delta}_t$ is the calculated trim-value, and K_p and K_i are tuning parameters. Here, it is important to not have too aggressive gains since this may lead the throttle to cut and surge. Therefore, the controller is tuned for an acceptable error, and then the integral term closes the error gap.

The controller from commanded pitch angle, θ_c, to elevator deflection, δ_e, is an $\mathcal{H}_\infty$ - controller. For the performance requirements, the acceptable overshoot is chosen to be $10\,\%$, while the frequency range is chosen to be $\omega_0 \in [1, 13.8]$[8]. First order tuning filters are used. As seen, symmetric icing does primarily affect the longitudinal dynamics, and icing can be classified as a low frequency disturbance. This mean that steady state error in pitch angle is expected when the UAV is subject to icing conditions. The main argumentation for still using first order filters for longitudinal direction is that as long as this steady state error is small enough and the disturbance response is not too slow, this error can be corrected for by an higher-level outer loop controller. The robust pitch controller parameters are summarized in table 2. The icing level for nominal plant used for the pitch controller synthesis was found to be $\zeta = 0.3$. This lead to an ν-gap of less than 0.31 to the worst case plants.

A similar approach is made for the gain-scheduled case. Here, a controller is selected if the icing level is within ± 0.1 of its nominal plant. The icing levels chosen are then $\zeta_{\text{nominal}} = \{0.1, 0.3, 0.5, 0.7, 0.9\}$. By using this tuning approach for gain-scheduling, the stability criterion is significantly relaxed, since the worst case icing levels are now defined $\zeta_{\text{nominal}} \pm 0.1$. The gain scheduled controllers are summarized in table 4. It is worth noticing that it is the frequency range that terminates the iterative process for all gain-scheduled pitch controllers. For simplicity, the gain-scheduled controller is only implemented with a simple switch, meaning when the icing level changes from the area of one controller to another, the controller is switched instantaneously. This may lead to undesired transients induced by the switching, which is why the gain-scheduled controller is used to investigate the performance improvement within the icing-area of one controller, rather than scenarios related to de-icing and ice accretion.

Lateral Control

The lateral controller sets the desired aileron deflection based on the commanded roll angle. The lateral state equation has the same structure as the longitudinal, in eq. (23), with state vector and inputs given as

$$\mathbf{x}_{\text{lat}} = \begin{bmatrix} v \\ p \\ r \\ \phi \end{bmatrix} \quad \mathbf{u}_{\text{lat}} = \delta_{\mathbf{a}}, \tag{25}$$

with v being the y-axis body-frame velocity, p the roll rate, r the yaw rate, ϕ the roll angle, and δ_a the aileron deflection.

The lateral open-loop dynamics of the UAV includes the roll rate damping mode, a spiral mode and the dutch roll mode, and is sensitive to asymmetric disturbances. Since one of the main objectives of the controllers is disturbance rejection, and coping with asymmetric conditions, the lateral controller is using a second-order sensitivity filter to increase the controller integral action. The steady state errors for the lateral controller in the asymmetric case were too large for the controller using first order tuning filter. The same iterative tuning process is performed for the lateral controller. Here, the performance requirements for overshoot is chosen to be $30\,\%$. It is important to notice that high integral action may lead to more oscillatory responses. One way to avoid this type of unwanted behaviour is to tighten the closed-loop robustness requirements. Here, the stability margin $s_m = 0.7$ is used. This is still within the area given by [14]. The frequency range is chosen to be $\omega_0 \in [1.0, 10.0]$. The lateral controller parameters are shown in table 3. The icing level for nominal plant uses for the lateral controller synthesis was found to be $\zeta = 0.3$. This lead to an ν-gap of less than 0.1 to the worst case plants. This gap is considerably lower than in the longitudinal case, which is a consequence

of symmetric icing conditions having its primarily effects on the longitudinal direction.

The same approach is repeated for the gain-scheduled controller. Here, the icing level resolution is chosen to be the same as for the longitudinal case, 0.2. I.e. a controller is selected of the icing level is within ± 0.1 if its nominal plant. The icing-levels chosen is then $\zeta_{\text{nominal}} = \{0.1, 0.3, 0.5, 0.7, 0.9\}$. The lateral gain scheduled controllers are summarized in table 5. The switching mechanism for the lateral controller is similar to the one described for the pitch controller.

4. Simulation results

In the following, three scenarios illustrate the performance of the presented controllers in various icing and wind conditions; response while maneuvering in different, constant icing levels, response to changing icing levels, and effects of wind gusts.

Constant icing levels—First, the gain-scheduled and the single $\mathcal{H}_\infty$ controllers are compared over a longitudinal and a lateral pre-determined sequences of maneuvers, for three different, constant icing levels; $\zeta \in \{0.0, 0.3, 1.0\}$, referred to as "clean", "some ice", and "iced".

The longitudinal test run is chosen to illustrate how the uav controller handles basic flight manoeuvres climb and level-flight, and is defined by the following sequence;

- Initial value at $\theta = 0°$
- Input ramp to $\theta = 20°$ with the slow rate ($2\,°/\text{s}$), followed by constant input angle for $10\,\text{s}$.
- Input ramp back to $\theta = 0°$ with the slow rate ($-2\,°/\text{s}$), followed by constant input angle for $10\,\text{s}$.
- Input ramp to $\theta = 10°$ with the fast rate ($10\,°/\text{s}$), followed by constant input angle for $10\,\text{s}$.
- Input ramp to $\theta = 0°$ with the fast rate ($-10\,°/\text{s}$), followed by constant input angle for $10\,\text{s}$
- Step input to $\theta = 10°$, followed by constant input for $15\,\text{s}$.
- Consecutive input steps between $\theta = 0°$ and $\theta = 10°$, with constant input angle for $2\,\text{s}$ in between each step.

The response in the longitudinal test runs are shown in fig. 7 and fig. 8 for the single- and the gain-scheduled robust controller, respectively. Both the percentage overshoot and settling time for the step at $62\,\text{s}$, plotted in fig. 6a, were improved by using gain-scheduling for all icing levels. The largest difference in settling time between the controllers is at icing level $\zeta = 1.0$, and is less than $1.5\,\text{s}$. The largest difference overshoot is at icing level $\zeta = 0.3$ and is less than 2.5 percentage points.

For all cases of ice, the roll angle tends to drift slowly away from the reference signal. This effect decreases with rising icing level, and is present in both controllers, albeit less for the gain-scheduled version. However, the drift is on a very low scale, and can easily be corrected by a higher-level guidance control loop. Other than this, the lateral directional variables do not depend on the longitudinal control, which is a direct result of the longitudinal/lateral decoupling in the model. The airspeeds and throttle time-series are very similar for both controllers.

The airspeed varies between 19.5 and 20.5 seconds. As the airspeed and pitch angle is strongly coupled, and hence the change in pitch angle is easily viewed on the changes in airspeed. As for the spikes in elevator deflection, a more rapid change in pitch angle gives a greater impact on the airspeed. When the pitch increases, the airspeed decrease and when pitch decreases, the airspeed increases. The airspeed controller tries to keep a constant airspeed at 20 m/s. This explains the shape of the throttle signal. In addition, increased icing leads to increased drag which requires a higher throttle signal to maintain airspeed. This explains why the throttle increases in magnitude when the icing level increases.

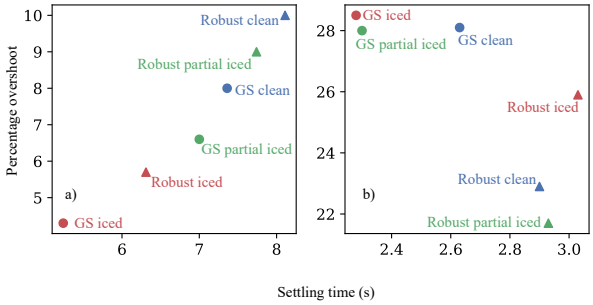

Figure 6. Settling time and percentage overshoot for the single- and the gain-scheduled robust controllers for the longitudinal (*a*)) and (*b*)) lateral directions. Settling time is defined from a $3\,\%$ error band.

The longitudinal test run for the gain-scheduled controller is shown in fig. 8. As for the single robust controller there is a small overshoot at all tested icing levels.

The lateral test run is chosen to illustrate how the uav controller handles the basic flight manoeuvres turning and level-flight, and is defined by the following sequence;

- Initial value at $\phi = 0°$.
- Input ramp to $\phi = 40°$ with the slow rate ($4\,°/\text{s}$), followed by constant input angle for $10\,\text{s}$.
- Input ramp to $\phi = -40°$ with the fast rate ($-10\,°/\text{s}$), followed by constant input angle for $10\,\text{s}$.
- Input step to $\phi = 0°$, followed by constant input angle for $10\,\text{s}$.
- Input step to $\phi = 20°$, followed by constant input angle for $15\,\text{s}$.
- Consecutive input steps between $\phi = -20°$ and $\phi = 20°$ followed by a constant input angle for $2\,\text{s}$ between each step.

The response in the lateral test runs are shown in figs. 9 and 10 for the single- and the gain-scheduled robust controller, respectively. A second-order filter with a maximum acceptable overshoot of $30\,\%$ was used in the roll tuning process. Hence, a quite large overshoot is as expected. As opposed to the longitudinal case, the overshoots at clean and some ice cases are quite similar, and the overshoot at the iced case is larger.

For both controllers, the angle of attack varies between 2.4 and 4.1 degrees during the test run, seen in fig. 9c and fig. 10. When the aircraft goes from a level flight in trim conditions to turning, the absolute value of the velocity component along the body frame z-direction will increase, which can be observed as an increase in the angle of attack. As expected, the direction of turn does not matter on the changes in the angle of attack. The variations increase with the icing level. Although the angle of attack and elevator deflection, seen in fig. 9e and fig. 10e, are similar across both controllers, the pitch response

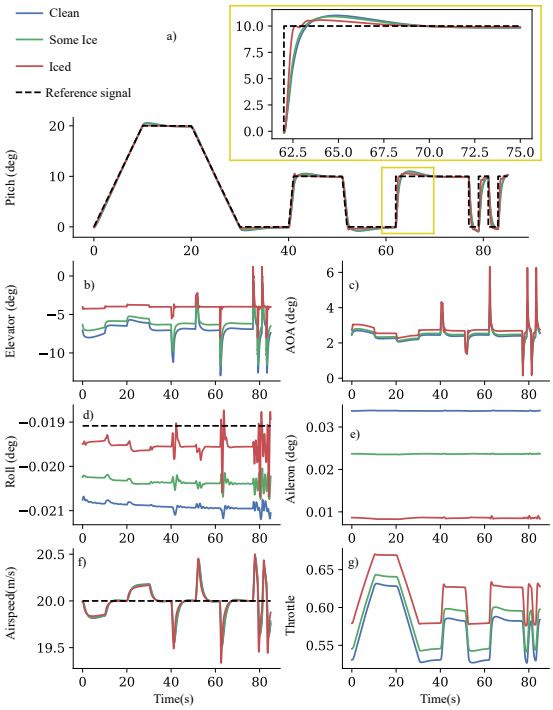

Figure 7. Single robust controller longitudinal test run, for different ice levels.

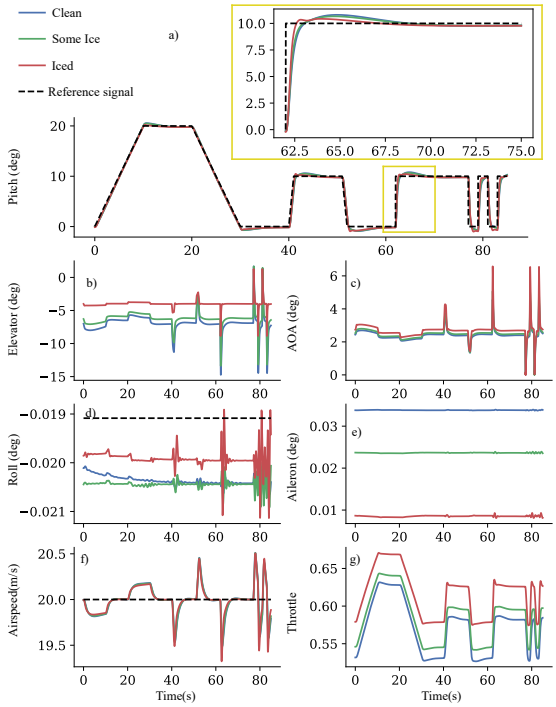

Figure 8. Gain-scheduled controller longitudinal test run, for different ice levels.

is different. This is most notable in the $\zeta = 1$ scenario, where the pitch response of the single robust controller in fig. 9 consistently has a lower error than in the other icing scenarios. However, this is not the case for the gain-scheduled controller, in fig. 10, where the pitch response is similar in all three icing conditions. This variation needs to be looked at in combination with the airspeed and throttle in fig. 9f and fig. 9g. Change in roll angle leads to change in airspeed. Note that these changes are quite small (± 0.06 m/s). The lateral controller gives more aggressive manoeuvres, leading to a higher degree of dependency between longitudinal and lateral directions, and thus larger spikes in pitch.

Time-varying icing conditions— In addition to testing the performance in different icing conditions, it is of interest to investigate the closed-loop dynamics in time-varying icing conditions induced by both the environment and by a de-icing system, [3]. The icing condition simulation cases are only simulated for the single robust controller, i.e. no gain scheduling. Two icing test runs are simulated. The first test run is illustrating the effects of instantaneous de-icing, and simulation results are compared for different airspeeds.

Case 1: commanded pitch, airspeed and roll are constant at trim conditions.
Case 2: initial icing level $\zeta = 1$.
Case 3: sudden symmetric ice removal from $\zeta = 1$ to $\zeta = 0$ after $3\,\mathrm{s}$.
Case 4: sudden symmetric change in icing level to $\zeta = 1$ after $10\,\mathrm{s}$.
Case 5: piecewise asymmetric ice removal after $20\,\mathrm{s}$. This simulates ice shedding during an inflight de-icing cycle. Here the icing on the left wing is $\zeta_{\text{left}} = 0$ and icing level on the right-wing is $\zeta_{\text{right}} = 0.5$ for $10\,\mathrm{s}$, followed by the right-wing icing going to $\zeta_{\text{right}} = 0.0$.

Figure 11 shows roll and pitch angles, where the illustrations on the top line of figure shows the icing level of the aircraft at each case. All transitions between cases happens instantaneously.

As expected, the roll angle is not noticeably affected by the symmetric change in ice after $3\,\mathrm{s}$. The roll angle is, however, very sensitive to the asymmetric icing disturbances after $20\,\mathrm{s}$ and $30\,\mathrm{s}$ seconds. This gives a disturbance response with a roll angle deflection at $10°$ and a slightly oscillatory decay back to the reference value within $4\,\mathrm{s}$. The pitch angle is highly dependant on both symmetrical and asymmetrical change of icing level. The disturbance response of the pitch angle is slower. The maximum error deflection occurs when the icing level goes from clean to worst-case mixed ice at $20\,\mathrm{s}$. This peak error is at approximately $2°$. The disturbance response goes slowly back to the reference value within $10\,\mathrm{s}$. The steady-state error is less than $0.3°$.

Figure 12 shows the deflection angle as a function of airspeed for the transitions between the cases. The first icing scenario is repeated with different airspeeds of $14\,\mathrm{m/s}$, $16\,\mathrm{m/s}$, $18\,\mathrm{m/s}$, $21\,\mathrm{m/s}$ and $24\,\mathrm{m/s}$. The purpose here is to look at how the de-icing procedure is affected by airspeed. Hence, the ice accretion case transition between case 2 and 3 is excluded from this figure. The tendency is quite clear; the disturbance deflection for both pitch angle and roll angles tend to decay when the airspeed rises. This rate of this decay gets smaller for higher airspeeds. For the lateral case in asymmetric icing, the roll angle deflection seems to go towards a constant when airspeed gets large, while for the longitudinal case, the pitch angle deflection seems to go towards 0.

The second test run considers a short performance test while the aircraft is in asymmetric condition, to simulate a defect in

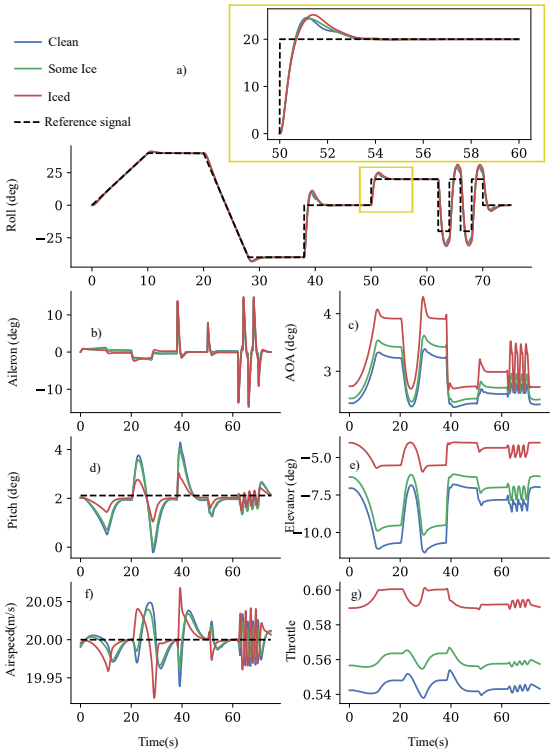

Figure 9. Single robust controller lateral performance test run, for different ice levels.

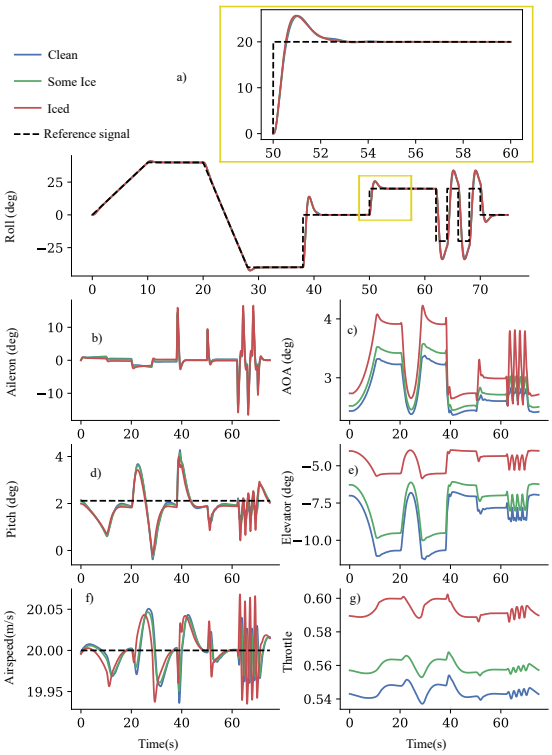

Figure 10. Gain-scheduled controller lateral test run, for different ice levels.

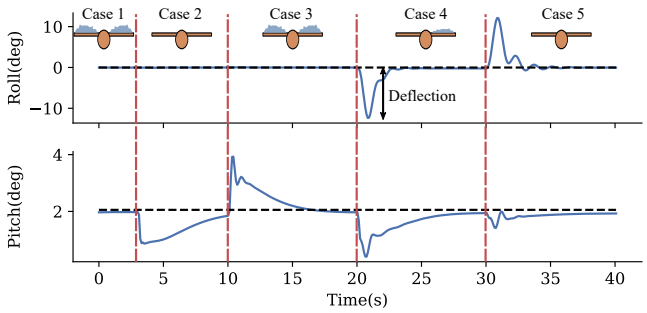

Figure 11. De-icing test run

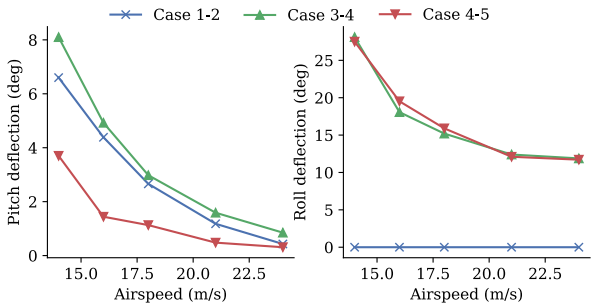

Figure 12. Comparison of de-icing deflections at different airspeed

the de-icing system on one of the wing;

- Commanded pitch, airspeed and roll are initially constant at trim conditions; $v_a = 21.4\,\mathrm{m/s}, \theta = 2.4°$, and $\phi = 0.0°$.
- Initial icing level $\zeta = 1$ on both wings.
- Initial step input to $\theta = 10°$, followed by constant pitch input for 10 s.
- Sudden asymmetric ice removal from $\zeta_{\text{left}} = 1$ to $\zeta_{\text{left}} = 0$ on the left wing after 3 s.
- Step input to $\theta = 0°$, followed by constant input for 10 s.
- Step input to $\phi = 20°$, followed by constant input for 10 s.
- Step input to $\phi = 0°$ constant input for 10 s.

Figure 13 shows the results of the second test run. As expected, the cross-coupling between longitudinal and lateral direction is increased with asymmetric icing. This can be seen in how the aerodynamic coefficients in the lateral direction depend on drag and lift force in fig. 2. By looking at the roll angle when a step is applied to the pitch angle, e.g. after 10 s. The pitch does also depend on the roll angle, but to a lower degree. This can be seen by looking at the pitch angle in fig. 13b when a step is applied to the roll angle. Figure 13c and fig. 13d show the icing level on the left and right-wing respectively. Figure 13e and fig. 13f show the aileron and elevator deflection. When subject to asymmetric icing, a significant aileron control effort is needed to keep the aircraft on a level flight. Given the flight configuration in this test run, the aileron deflection required to maintain level flight is about 10°. Hence, asymmetric icing limits the ability to perform aggressive lateral manoeuvring and can easily cause saturation of the control signal. The saturation limit of the control signal will also give an upper threshold to the degree of asymmetry that can be handled by the uav. Figure 13g and fig. 13h show the airspeed and throttle, for completeness.

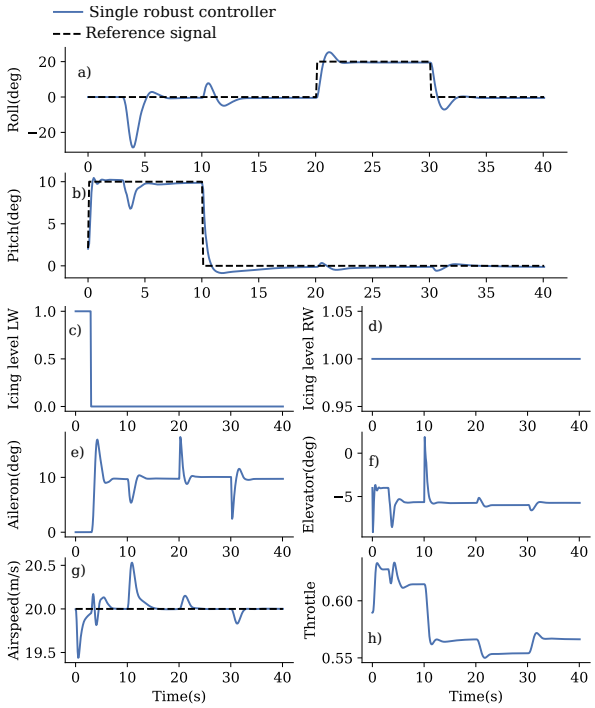

Figure 13. Performance test run with asymmetric icing

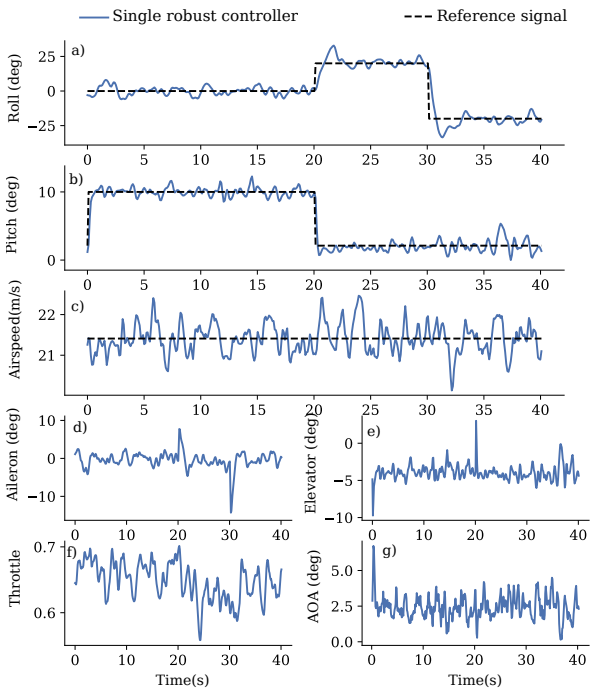

Figure 14. Single robust controller wind condition test run.

Performance in wind gust

A short performance test is simulated to verify the single robust controllers' ability to track references in wind conditions. Compensation for constant winds is commonly handled within the higher-level guidance controller rather than in the low level stabilizing inner-loop controllers. Therefore, this simulation is only looking at the wind gusts using the Dryden gust model[5] of moderate intensity[3]. The simulation sequence used in wind conditions is;

- Initial value at $\theta = \phi = 0°$.
- Step input to $\theta = 10°$, followed by constant input for 10 seconds.
- Step input to $\theta = 0°$ and a simultaneous step input to $\phi = 20°$, followed by constant input for 10 s.
- Step input to $\phi = -20°$, followed by constant input for 10 s.

The resulting response of the UAV in fig. 14 show that the controller tracks the reference well, in general, although the oscillations around the reference are more pronounced compared to the previous simulations. In order to quantify the ability to reject wind gust disturbances, the integral of the absolute value of the error,

$$\text{ie} = \int_{t_0}^{t} |e(t)|dt, \tag{26}$$

is introduced. For the longitudinal case, the integral error is 42.31, while for the lateral case, the integral error is 105.72.

[3] *Moderate* means that the wind gusts are of an intensity that is typically encountered in steady winds of 30 kn

5. Conclusion

Two types of inner-loop controllers based on $\mathcal{H}_\infty$ optimal control were implemented and tested; a single robust controller and a gain-scheduled controller. In order to mitigate the effects of icing, both controllers fulfilled closed-loop requirements to ensure stability and robustness to model uncertainty. The simulation results showed that both controller types gave satisfactory results in terms of robustness, stability and performance. From the performance comparison of the two controller types, one can conclude that by increasing the information available and assuming that the level of icing is known, the performance in terms of settling time and overshoot is improved by using a gain scheduled controller. In another test scenario, in-flight de-icing was performed using the single robust controller for different levels of airspeed. the tendency was clear; higher airspeed within the tested range of reasonable UAV airspeeds minimizes the disturbance related to instantaneous removal of ice.

How the dynamic modes of a Skywalker X8 fixed-wing UAV are affected by icing conditions was investigated based on a simulation model where icing is modelled using linear interpolation between base aircraft without ice and the worst-case mixed ice configuration.

Appendix: Controller parameters

The selected point of attack locations of the aerodynamic forces are given in table 1. The tuning parameters for the

Table 1. Aerodynamic forces points of attack

$y_{D,r}$	0.25 m
$y_{L,r}$	0.4 m
$y_{S,r}$	0.2 m

airspeed controller, eq. (24), are based on trial-error tuning, where $k_p = 0.068$ and $k_i = 0.057$ is found suitable.

Table 2. Longitudinal robust controller summary

Filter parameter	Value
ω_0	6.2 rad/s
m	2
a	0.001
w_c	1
Performance parameter	**Value**
γ^*_{lon}	1.9617

Table 3. lateral robust controller summary

Filter parameter	Value
ω_0	2.1 rad/s
m	2
a	0.0002
w_c	1
Performance parameter	**Value**
γ^*_{lon}	1.9199

Table 4. Longitudinal gain scheduled controllers with icing level value ζ

ζ	γ^*_{lat}	ω_0 (rad/s)	m	a	w_c
0.1	3.6298	13.8	2	0.001	1.0
0.3	3.5165	13.8	2	0.001	1.0
0.5	3.3971	13.8	2	0.001	1.0
0.7	3.2827	13.8	2	0.001	1.0
0.9	3.1956	13.8	2	0.001	1.0

Table 5. Lateral gain scheduled controllers with icing level value ζ

ζ	γ^*_{lat}	ω_0 (rad/s)	m	a	w_c
0.1	2.1699	2.9	2	0.002	1.0
0.3	2.2860	3.2	2	0.002	1.0
0.5	2.3216	3.3	2	0.002	1.0
0.7	2.2860	3.2	2	0.002	1.0
0.9	2.3128	3.2	2	0.002	1.0

ACKNOWLEDGMENTS

This work was supported by the Norwegian Research Council through IKTPLUSS project grant no. 316425, and the Centre of Autonomous Marine Operations and Systems (NTNU-AMOS) at the Norwegian University of Science and Technology (grant no. 223254).

REFERENCES

[1] R. Hann and T. A. Johansen, "Unsettled topics in unmanned aerial vehicle icing," Society of Automotive Engineers (SAE) Edge Report, Tech. Rep., 2020.

[2] ——, "UAV icing: The influence of airspeed and chord length on performance degradation," *Aircraft Engineering and Aerospace Technology*, vol. 93, pp. 832–841, 2021.

[3] R. Hann, A. Enache, M. C. Nielsen, B. N. Stovner, J. van Beeck, T. A. Johansen, and K. T. Borup, "Experimental heat loads for electrothermal anti-icing and de-icing on UAVs," *Aerospace*, vol. 8, no. 3, p. 83, 2021.

[4] A. Winter, R. Hann, A. Wenz, and T. A. Johansen, "Stability of a Flying Wing UAV in Icing Conditions," *8th European Conference for Aeronautics and Space Sciences (EUCASS)*, 2019.

[5] R. W. Beard and T. W. McLain, *Small unmanned aircraft: Theory and practice*. Princeton university press, 2012.

[6] K. Gryte, R. Hann, M. Alam, J. Rohac, T. A. Johansen, and T. I. Fossen, "Aerodynamic modeling of the Skywalker X8 Fixed-Wing Unmanned Aerial Vehicle," *2018 International Conference on Unmanned Aircraft Systems, ICUAS 2018*, pp. 826–835, 2018.

[7] C. Deiler, "Aerodynamic modeling, system identification, and analysis of iced aircraft configurations," *Journal of Aircraft*, vol. 55, no. 1, pp. 145–161, 2018.

[8] E. Lavretsky and K. A. Wise, "Robust adaptive control," in *Robust and adaptive control*, Springer, 2013, pp. 317–353.

[9] G. Vinnicombe, *Uncertainty and Feedback: H_∞ loop-shaping and the ν-gap metric*. World Scientific, 2001.

[10] S. Skogestad and I. Postlethwaite, *Multivariable feedback control: analysis and design*. Citeseer, 2007, vol. 2.

[11] K. Glover and J. C. Doyle, "State-space formulae for all stabilizing controllers that satisfy an H_∞-norm bound and relations to relations to risk sensitivity," *Systems & Control Letters*, vol. 11, no. 3, pp. 167–172, 1988. [Online]. Available: `http://www.sciencedirect.com/science/article/pii/0167691188900552`.

[12] K. J. Åström, "Adaptive control," in *Mathematical System Theory: The Influence of R. E. Kalman*, A. C. Antoulas, Ed. Berlin, Heidelberg: Springer Berlin Heidelberg, 1991, pp. 437–450. [Online]. Available: `https://doi.org/10.1007/978-3-662-08546-2_24`.

[13] K. Zhou and J. C. Doyle, *Essentials of robust control*. Prentice Hall Upper Saddle River, NJ, 1998, vol. 104.

[14] K. J. Åström and R. M. Murray, *Feedback systems: an introduction for scientists and engineers*. Princeton university press, 2010.

BIOGRAPHY

Ruben Kleiven *Ruben Kleiven received his MSc in Engineering Cybernetics in 2021 from the Norwegian University of Science and Technology (NTNU), with Guidance, Navigation and Control as his main field of study. He is currently working as an embedded software developer for Kongsberg Maritime.*

Kristoffer Gryte *received his MSc and PhD in Engineering Cybernetics in 2015 and 2020, respectively, both from the Norwegian University of Science and Technology (NTNU). He currently works as a researcher on software for autonomus systems at NTNU. His research interests currently evolve around mobile robots, particularly aerial, including guidance, navigation and control.*

Tor Arne Johansen *received the MSc degree in 1989 and the PhD degree in 1994, both in electrical and computer engineering, from the Norwegian University of Science and Technology, Trondheim, Norway. From 1995 to 1997, he worked at SINTEF as a researcher before he was appointed Associated Professor at the Norwegian University of Science and Technology in Trondheim in 1997 and Professor in 2001. He has published several hundred articles in the areas of control, estimation and optimization with applications in the marine, aerospace, automotive, biomedical and process industries. In 2002 Johansen cofounded the company Marine Cybernetics AS where he was Vice President until 2008. Prof. Johansen received the 2006 Arch T. Colwell Merit Award of the SAE, and is currently a principal researcher within the Center of Excellence on Autonomous Marine Operations and Systems (NTNU-AMOS) and director of the Unmanned Aerial Vehicle Laboratory at NTNU and the SmallSat Laboratory at NTNU. He recently co-founded the spin-off companies Scout Drone Inspection, UBIQ Aerospace and Zeabuz.*